Radiative Effect on Particle Acceleration via Relativistic Electromagnetic Expansion

K. Noguchi*, E. Liang
Rice Univ. TX 77005 USA

The radiation damping effect on the diamagnetic relativistic pulse accelerator (DRPA) is studied in two-and-half dimensional Particle-in-Cell (PIC) simulation with magnetized electron-positron plasmas. Self-consistently solved radiation damping force converts particle energy to radiation energy. The DRPA is still robust with radiation, and the Lorentz factor of the most high energy particles reach more than two thousand before they decouple from the electromagnetic pulse. Resulted emitted power from the pulse front is lower in the radiative case than the estimation from the non-radiative case due to the radiation damping. The emitted radiation is strongly linearly polarized and peaked within few degrees from the direction of Poynting flux.

1. INTRODUCTION

Radiation loss and damping can become important in the plasma energetics and dynamics when charged particles suffer extreme acceleration. In the ultra-relativistic regime, the accumulated effect from radiation damping can severely limit individual particle acceleration even if the radiation damping force is weak compared to external forces. However, conventional Particle-in-Cell simulations of collisionless plasmas have not included radiation effects. We developed a new 2-1/2-D code including self-consistent radiation damping, and studied a effect of radiation damping in particle acceleration driven by relativistic pulse accelerator (DRPA) [1] in the strong magnetic field limit. From the radiation-damped plasma and field evolution, we obtained the observable high energy radiation output. This radiative PIC simulation code is applicable to to a wide range of high-energy astrophysics phenomena (pulsars, blazars, gamma-ray bursts) and ultra-intense laser applications [2].

The outline of this paper is as follows. In Sec. 2, the derivation of the radiation damping force in the relativistic form is shown. In Sec. 3 we explain how the radiation damping force is implemented into the PIC code. Results of simulation and comparison with non-radiative case are given in Sec. 4, and we summarize in Sec. 5.

2. DERIVATION OF RADIATIVE FORCE

In the conventional PIC simulations, radiation damping force $\boldsymbol{f}_{rad}$ is ignored because of its small amplitude compared to external forces $\boldsymbol{F}_{ext}$. However, it is not negligible when the accumulated work done by the radiation damping during deceleration time τ_{decl} is comparable to the work done by the external force in typical acceleration time [2].

It is impractical to include high-frequency radiation wave into the electromagnetic calculation in the PIC code, since the typical radiation wavelength is much shorter than the spatial resolution of the fields ($\sim$ Debye length $\lambda_D \equiv c/\omega_{pe}$, where $\omega_{pe} = \sqrt{4\pi\rho e/m_e}$ is the electron plasma frequency). Accelerated particles can emit up to the critical frequency $\omega_c = 3\gamma^2\Omega_{ce}$, where $\gamma = E/m_e c^2 = 1/\sqrt{1 - v^2/c^2}$ is the Lorentz factor and $\Omega_{ce} = eB/(m_e c)$ is the electron gyro-frequency. The ratio of the critical radiation wavelength λ_c to λ_D is given by $\lambda_c/\lambda_D = (2\pi\omega_{pe})/(3\gamma^3\Omega_{ce})$, which is $\ll 1$ because $\omega_{pe}/\Omega_{ce} < 0.1$ in magnetic-dominated cases and $\gamma \gg 1$.

Instead, we introduce a radiation damping force in the form of the Dirac-Lorentz equation [3], which is proven to be exact for a classical point particle [4]. The 4-vector form of Dirac-Lorentz equation with the damping force g^i is given by

$$mc\frac{du^i}{ds} = \frac{e}{c}F^{ik}u_k + g^i, \tag{1}$$

where F^{ik} is the electromagnetic tensor [5], u^i is the velocity four-vector, and g^i is the radiation damping force

$$g^i = \frac{2e^2}{3c}\left(\frac{d^2u^i}{ds^2} - u^i u^k \frac{d^2u_k}{ds^2}\right), \tag{2}$$

which satisfies the auxiliary relation $g^i u_i = 0$. Since Eq. (2) includes the second derivative of u^i, there exist unphysical run-away solutions [5]. To avoid the run-away solutions, we assume $g_i \ll eF^{ik}u_k/c$ and eliminate the second derivative terms in g^i by expressing d^2u^i/ds^2 with the first derivative of Eq. (1) with $g^i = 0$,

$$\frac{d^2u^i}{ds^2} = \frac{e}{mc^2}\frac{\partial F^{ik}}{\partial x^l}u_k u^l + \frac{e^2}{m^2c^4}F^{ik}F_{kl}u^l. \tag{3}$$

Using the fact $(\partial F^{ik}/\partial x^l)u_i u_k = 0$, we find

$$g^i = \frac{2e^3}{3mc^3}\left[\frac{\partial F^{ik}}{\partial x^l}u_k u^l - \frac{e}{mc^2}F^{il}F_{kl}u^k\right.$$

*noguchi2@llnl.gov

$$+\frac{e}{mc^2}(F_{kl}u^l)(F^{km}u_m)u^i\Big]. \qquad (4)$$

The resulting damping force term $\boldsymbol{f}_{rad}$ in the 3-vector form is given by [3]

$$\begin{aligned}\boldsymbol{f}_{rad} = & \frac{2e}{3\Omega_{ce}}k_{rad}\times \\ & \left\{\gamma\left[\left(\frac{\partial}{\partial t}+\boldsymbol{v}\cdot\nabla\right)\boldsymbol{E}+\frac{\boldsymbol{v}}{c}\times\left(\frac{\partial}{\partial t}+\boldsymbol{v}\cdot\nabla\right)\boldsymbol{B}\right]\right. \\ & +\frac{e}{mc}\left[\boldsymbol{E}\times\boldsymbol{B}+\frac{1}{c}\boldsymbol{B}\times(\boldsymbol{B}\times\boldsymbol{v})+\frac{1}{c}\boldsymbol{E}(\boldsymbol{v}\cdot\boldsymbol{E})\right] \\ & \left.-\frac{e\gamma^2}{mc^2}\boldsymbol{v}\left[\left(\boldsymbol{E}+\frac{1}{c}\boldsymbol{v}\times\boldsymbol{B}\right)^2-\frac{1}{c^2}(\boldsymbol{E}\cdot\boldsymbol{v})^2\right]\right\}, \qquad (5)\end{aligned}$$

where $\boldsymbol{v}$ is the 3-velocity, and $\boldsymbol{E}$ and $\boldsymbol{B}$ are the self-consistent electric and magnetic fields. Here we introduce a non-dimensional factor k_{rad} given by

$$k_{rad}=\frac{r_e\Omega_{ce}}{c}=1.64\times10^{-16}\times B(\text{gauss}), \qquad (6)$$

where $r_e = e^2/(mc^2)$ is the classical electron radius.

The first term of the radiation damping force (5) represents the radiation damping due to the ponderomotive force acceleration. The third term is Compton scattering by large scale ($\lambda > \lambda_D$) electromagnetic field which reduces to Thomson scattering in the classical limit [6]. Note here that the scattering between radiation field and particles is not considered since electromagnetic field in Eq. (5) is averaged over the grid separation that is much larger than the wavelength of radiation, as we discussed above. In other words, plasma is perfectly transparent to emitted radiation, and all the radiation disappears from the simulation box immediately after particles radiate.

The magnetic field strength of pulsars are in the range of $10^{-4} \le k_{rad} \le 10^{-3}$, and $k_{rad} \simeq 10^{-2}$ for magnetars. In the laboratory, $k_{rad} \simeq 10^{-6}$ $(I/10^{22}\text{Wcm}^{-2})^{1/2}$ for lasers of intensity I. Hence for ultraintense laser interactions ($I \ge 10^{22}\text{Wcm}^{-2}$), radiation damping effects can become significant on simulation time scales $>$ 0.3ps ($= 10^5\Omega_{ce}^{-1}$). (See also [2]) In our simulation, we can enhance the radiation effect by increasing the value of k_{rad}, or the 'effective' electron radius. However, we should restrict ourselves not to reach the quantum-limit, $\hbar\Omega_{ce} \sim m_ec^2$ or $B > 4.4\times10^{13}$ gauss, which corresponds to $k_{rad} = 7.2\times10^{-3}$, or the Dirac-Lorentz equation (1) fails. We choose k_{rad} from zero to 10^{-3} in the simulation to enhance the radiation effect and $|\boldsymbol{f}_{rad}|\tau_{sim} \simeq |\boldsymbol{F}_{ext}|\Omega_{ce}^{-1}$ so we can see the difference between radiative and non-radiative ($k_{rad} = 0$) case within the simulation time-scale $\tau_{sim} \simeq 10^4\Omega_{ce}^{-1}$.

3. IMPLIMENTATION OF RADIATION FORCE

The 2-1/2D explicit PIC simulation scheme is used with the explicit leap-frogging method for time advancing [7]. Spacial grids for the fields are uniform in both x and z directions, $\Delta x = \Delta z = \lambda_D$. The simulation domain in the x–z plane is $-L_x/2 \le x \le L_x/2$ and $0 \le z \le L_z$ with a doubly periodic boundary condition in both directions.

Following Liang et. al. [1], the initial plasma is uniformly distributed at the center of the simulation box, $-6\Delta x < x < 6\Delta x$ and $0 < z < L_z$. The background uniform magnetic field $\boldsymbol{B}_0 = (0, B_0, 0)$ is applied only in the same region, so that the magnetic field freely expands toward the vacuum regions, $x > 6\Delta x$ and $x < -6\Delta x$ with accelerating plasma. We choose L_x to be long enough so that plasma and EM wave never hit the boundaries in the x direction within the simulation time.

The initial temperature of plasma is assumed to be a spatially uniform relativistic Maxwellian, $k_BT_e = k_BT_p = 1$MeV, where the subscripts e and p refer to electrons and positrons.

The radiation damping force (5) is calculated self-consistently and fully-explicitly as follows. The velocity of each particle should be updated each time step from $\boldsymbol{v}(t-\Delta t/2)$ to $\boldsymbol{v}(t+\Delta t/2)$, using the electromagnetic field and $\boldsymbol{f}_{rad}$ at time t following the equation of motion in the relativistic form,

$$\frac{d\boldsymbol{p}}{dt}=e\boldsymbol{E}+\frac{e}{c}\boldsymbol{v}\times\boldsymbol{B}+\boldsymbol{f}_{rad}, \qquad (7)$$

where $\boldsymbol{p} = m\gamma\boldsymbol{v}$ is the relativistic momentum. All the terms in the equation (5) are given by the ordinary leap-frog field solver except $d\boldsymbol{E}(t)/dt$ term, which is not calculated at time t in the conventional PIC code.

In order to calculate $d\boldsymbol{E}(t)/dt$, we need to know $\boldsymbol{J}(t)$. First, we advance the position $\boldsymbol{x}$ half timestep from $t - \Delta t/2$ to t for each particle using velocity $\boldsymbol{v}(t - \Delta t/2)$. Next, temporal current $\boldsymbol{J}_t(t)$ is calculated from $\boldsymbol{v}(t - \Delta t/2)$ and $\boldsymbol{x}(t)$. Note that this current $\boldsymbol{J}_t(t)$ is not exact because of the velocity field not at time t but $\boldsymbol{v}(t - \Delta t/2)$. Finally, the term $d\boldsymbol{E}(t)/dt$ is calculated using the Maxwell equation, and the radiation damping force is calculated for each particle. To update the velocity, we consider a sum of the radiation force and the electric field force as a net 'acceleration' force, and apply the Boris method for particle gyration [7].

4. RESULTS

We choose six different sets of parameters shown in Table I, by changing $k_{rad} = 0$, 10^{-4}, 10^{-3} and $\omega_{pe}/\Omega_{ce} = 0.1$, 0.01, and run simulations for each case.

Table I Parameters for each runs

	k_{rad}	ω_{pe}/Ω_{ce}	Duration $t\Omega_{ce}$
Run A	0	0.1	10000
Run B	10^{-4}	0.1	10000
Run C	10^{-3}	0.1	10000
Run D	0	0.01	70000
Run E	10^{-4}	0.01	70000
Run F	10^{-3}	0.01	70000

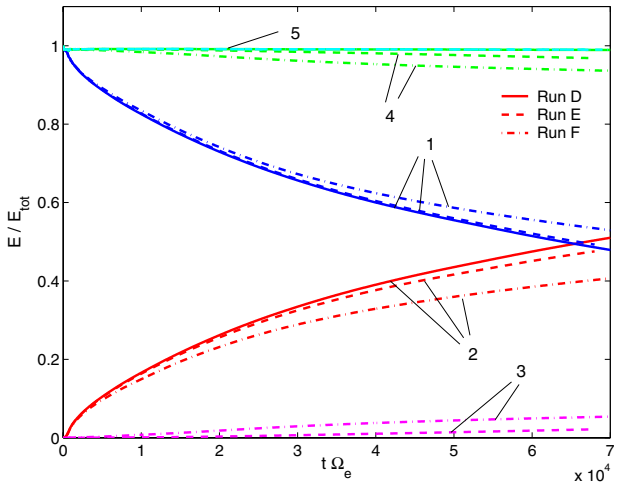

Figure 1: System-integrated energy in the electromagnetic field (1), particles (2), radiation damping (3), sum of field and particle energy (4), and total energy (5) functions of time for Run D (solid), E (dashed) and F (dash-dot).

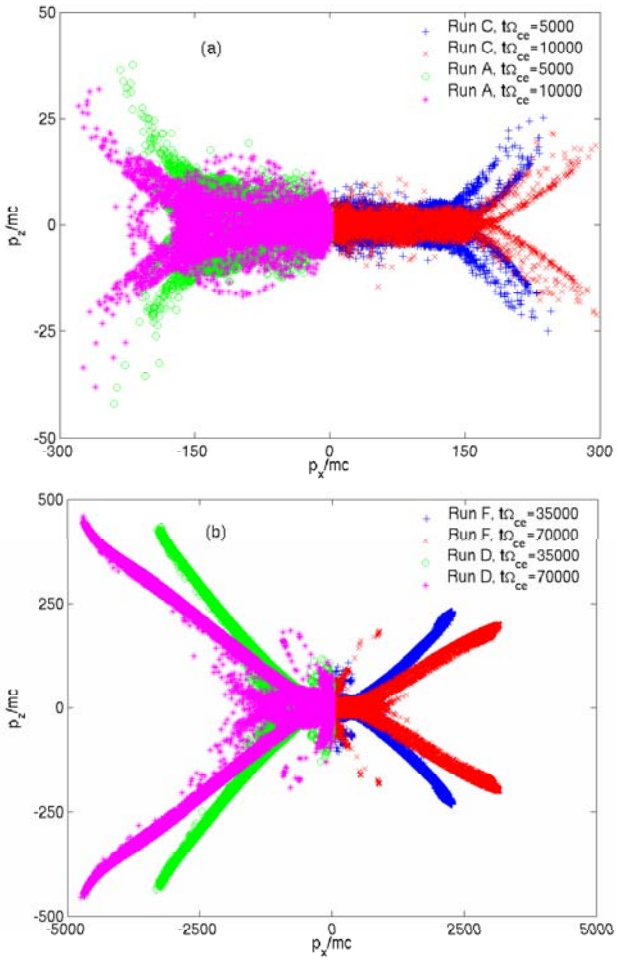

Figure 2: Momentum distribution of particles for Run A [(a), $x < 0$] and Run C [(a), $x > 0$] at $t\Omega_{ce} = 5000$ (green, blue) and $t\Omega_{ce} = 10000$ (magenta, red), and Run .D [(b), $x < 0$] and Run F [(b), $x > 0$] at $t\Omega_{ce} = 35000$ (green, blue) and $t\Omega_{ce} = 70000$ (magenta, red). Results in the positive and negative x directions are identical in all cases.

Hereafter, we call Run A-C as the weak magnetic field case and Run D-F as the strong magnetic field case, based on the ratio ω_{pe}/Ω_{ce}.

First, we check the total energy conservation for Run D,E and F in Fig. 1. In the radiative (RD) cases, the energy loss by the radiation E_{rad} is obtained from the time integral

$$E_{rad}(t) = \int_0^t \left(\sum_{e,p} \boldsymbol{v}(t') \cdot \boldsymbol{f}_{rad}(t') \right) dt'. \qquad (8)$$

In the non-radiative (NRD, $k = 0$) case, total energy of the system is given by the sum of the field energy E_{fie} (Line 1) and kinetic energy E_{kin} (Line 2), and it conserves. In the RD case, however, sum of E_{kin} and E_{fie} does not conserve (Line 4), but sum of E_{kin}, E_{fie} and the radiation energy E_{rad} (Line 3) conserves (Line 5), indicating that the radiation damping force is self-consistently calculated. In all the RD cases, the energy is transferred from field to particle, and then radiation, indicating the DRPA mechanism accelerates particles even in the RD cases. Energy transfer, however, from field to particles becomes less efficient with larger radiation damping force. Radiation prevents energetic particles to get accelerated from EM field, resulting less efficiency of transfer in high energy tail of the particle distribution.

Figure 2 shows the momentum distribution of particles for (a) Run A($x < 0$) and Run C($x > 0$), and (b) Run D($x < 0$) and Run F($x > 0$). The DRPA accelerates electrons and positrons in the same direction along the x axis, whereas electric field E_z accelerates electrons in the positive z and positrons in the negative z direction respectively in the positive x region. In the negative x region, acceleration directions are opposite for both species, forming X shape distribution in the $p_x - p_z$ plane as a result. Charge separation does not occur because of the periodicity in the z direction. Resulted induced current J_z accelerates particles in the x direction by the ponderomotive force $\boldsymbol{J} \times \boldsymbol{B}$. The ponderomotive force creates successive 'potential wells' in the x direction, which captures

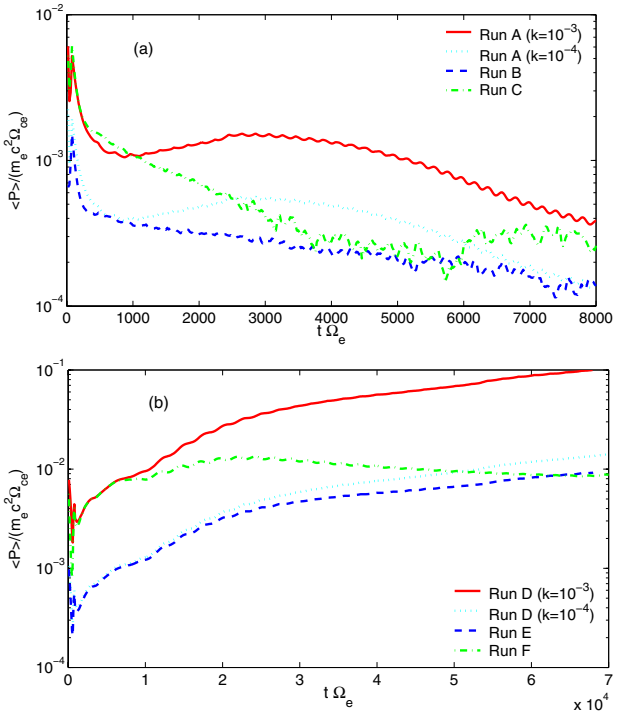

Figure 3: Average instantaneous radiation power from particles within $30\lambda_D$ from pulse front for (a) $\omega_{pe}/\Omega_{ce} = 0.1$ and (b) 0.01 with $k_{rad} = 1-^{-3}$ (dash-dot line) and $k_{rad} = 10^{-4}$ (dashed line). Estimated power for NRD cases with $k_{rad} = 10^{-3}$ (solid line) and 10^{-4} (dotted line) are also shown for comparison.

and accelerates co-moving particles. We emphasize here that there is no charge separation in the x direction because of no mass difference between electron and positron.

Obviously, particle momenta in both x and z directions are radiated away in the RD cases in both weak and strong magnetic field cases. Bifurcation in high energy tails occurs in Run C since slow particles can not keep up with the speed of the first (and the fastest) ponderomotive potential well and decoupled from it. Then the second potential well captures these slow particles and accelerates them again, which creates the bifurcated high energy tails in the phase space. The bifurcation is less clear in Run A than Run C because energetic particles are not suffered from the radiation damping and most of them can stay in the first potential well.

In the strong magnetic field case [Fig. 2(b)], acceleration is strongly reduced in the RD case (Run F). For high energy ($\gamma \gg 1$) particles, the Compton scattering [the third term in Eq. (5)] becomes a dominant term because of the large Lorentz factor, and makes the DRPA acceleration less efficient. Bifurcation is strongly suppressed in both Run D and F, since the first potential well is deep enough to capture almost all of the energetic particles.

Next, we compare the radiation power of RD cases with NRD cases. For the NRD case, we estimate the radiation power using the relativistic dipole formula [6]

$$\langle P \rangle = \frac{2}{3}\frac{k_{rad}}{m\Omega_{ce}}(F_\parallel^2 + \gamma^2 F_\perp^2), \tag{9}$$

where $F_\parallel$ and $F_\perp$ are the parallel and perpendicular components of the force with respect to the particle's velocity. The bracket $\langle\rangle$ indicates that we take the average of all the particles locating within $30\lambda_D$ from the pulse front, and the number of particles within this layer decreases with time because of the decoupling from the EM pulse. Since Eq. (9) is proportional to k_{rad}, we plot Run A and D with $k = 10^{-3}$ and 10^{-4} to compare with the other four RD cases.

For the RD cases, the radiation power is calculated using the formula

$$\langle P \rangle = |\boldsymbol{f}_{rad} \cdot \boldsymbol{v}|. \tag{10}$$

We compared the result of these two formulae for the RD cases,and they matched within the linewidth.Therefore, We only show the result of Eq. (10) here.

Figure 3 shows the instantaneous radiation power $\langle P \rangle$ for all runs. The initial peak around $t\Omega_{ce} = 100$ is due to thermal-cyclotron emission [6], and the estimated radiation power for the NRD case quantitatively matches with the RD case. At a later time ($t\Omega_{ce} > 1000$), however, more power is irradiated in the NRD cases than in the RD cases, because energetic particles are continuously accelerated without losing their energy self-consistently in the NRD cases. In the RD cases, however, all the energetic particles are decelerated by the radiation damping, and the instant radiation power decreases caused by slower velocity and smaller damping force.

Finally, we calculate the radiation field and its angular dependence self-consistently using the velocity and acceleration of each particle. Intensity I and polarization Π of the radiation received by the observer located at $\boldsymbol{x}$ are given by [5, 6]

$$I(\hat{\boldsymbol{n}}, \tau) = \sum_i \left[|\boldsymbol{E}_i|^2\right]_{\rm ret}, \tag{11}$$

and

$$\begin{aligned} E_y^2(\hat{\boldsymbol{n}}, \tau) &= \sum_i \left[|\boldsymbol{E}_i \cdot \hat{\boldsymbol{y}}|^2\right]_{\rm ret}, \\ E_z^2(\hat{\boldsymbol{n}}, \tau) &= \sum_i \left[|\boldsymbol{E}_i \cdot \hat{\boldsymbol{z}}|^2\right]_{\rm ret}, \\ U(\hat{\boldsymbol{n}}, \tau) &= 2\sum_i \left[(\boldsymbol{E}_i \cdot \hat{\boldsymbol{y}})(\boldsymbol{E}_i \cdot \hat{\boldsymbol{z}})\right]_{\rm ret}, \qquad (12) \\ \Pi(\hat{\boldsymbol{n}}, \tau) &= \frac{\sqrt{(E_z^2)^2 + (E_y^2)^2 - 2E_y^2E_z^2 + U^2}}{E_z^2 + E_y^2}, \qquad (13) \end{aligned}$$

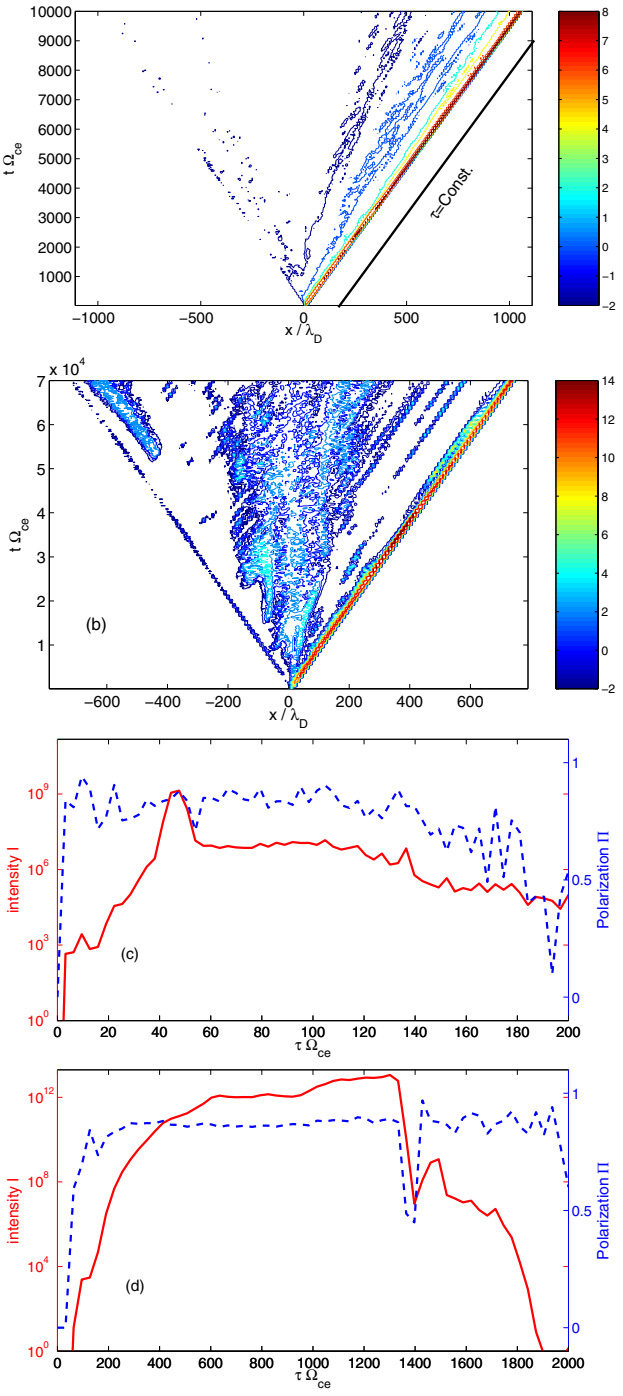

Figure 4: Contour plots of instantaneous intensity $\log_{10} I$ as a function of local time t for $\theta = \phi = 0$ for (a) Run C and (b) Run F, and intensity (red lines, right scales) and polarization (blue lines, left scales) as functions of observational time τ for (c) Run C and (d) Run F. Intensity is in arbitrary scale. To obtain time dependence of intensity, instantaneous intensity from each particle is summed up along the light cone $\tau = t - R/c$ =const., shown as a black dotted line in panel (a). The light cone moves horizontally leftward with τ.

where

$$\boldsymbol{E}_i = \frac{e}{c}\frac{\hat{\boldsymbol{n}} \times [(\hat{\boldsymbol{n}} - \boldsymbol{\beta}_i) \times \dot{\boldsymbol{\beta}}_i]}{(1 - \hat{\boldsymbol{n}} \cdot \boldsymbol{\beta})^3 R}, \tag{14}$$

is the radiated electric field from particle i located at $\boldsymbol{r}$, $\hat{\boldsymbol{n}}$ is a unit vector in the direction of $\boldsymbol{x} - \boldsymbol{r}(\tau)$, $\boldsymbol{\beta} = \boldsymbol{v}(\tau)/c$, and $\dot{\boldsymbol{\beta}} = d\boldsymbol{\beta}/dt$. We assume that $|\boldsymbol{x}| \gg |\boldsymbol{r}|$ so that $\hat{\boldsymbol{n}}$ is parallel to $\boldsymbol{x}$. The square brackets with a subscript "ret" mean that the quantity in the brackets is evaluated at the retarded time $\tau = t - R/c$, where $R = |\boldsymbol{x} - \boldsymbol{r}|$. To specify the direction of the observer with respect to the x axis, we introduce θ and ϕ as

$$\hat{\boldsymbol{n}} = (\cos\theta\cos\phi, \cos\theta\sin\phi, \sin\theta). \tag{15}$$

In Figs. 4(a) and (b), the contour plot of instantaneous intensity before taking the summation over the retarded time is plotted, as a function of local time t with $\phi = \theta = 0$, illustrating the ray-tracing technique used in Eqs. (11) and (12). We take a sum of intensity along the light cone $\tau = t - R/c$ =const., which is indicated as a black line, up to $t\Omega_{ce} = 10000$ for Run C and $t\Omega_{ce} = 70000$ for Run D. The light cone moves toward the negative x direction with τ, and we take $\tau = 0$ when the pulse front reaches to the observer. Since all the particles cross the light cone τ =const. only once, we take a sum of I and Π as follows. First, we follow the trajectory of each particle, and store their instantaneous intensity. When each particle crosses the light cone $\tau\Omega_{ce} = 1$, we take the average of the instantaneous intensity of the particle over the trajectory between $\tau\Omega_{ce} = 0$ and 1, and add it to the intensity I. Then we continue to follow the particle trajectory and sum up the intensity again until it hits the next light cone. We continue the summation until the signal in the initial plasma thickness reaches to the observer, $\tau = 12\lambda_D/c$, We also note that the intensity is extremely asymmetric because only energetic particles accelerated in positive x direction can radiate strong emission to the observer.

The time dependence of intensity and polarization with $\phi = \theta = 0$ is shown in Figs. 4(c) and (d). If all the particle moves with the speed of light and are continuously accelerated toward the direction of $\hat{\boldsymbol{n}}$, all the radiation emitted from particles should reach the observer at the same time and the signal becomes a δ-function pulse. However, energetic particles are bouncing back and forth within the ponderomotive potential well, and slower particles are dropped off to the next well, which broaden the spatial distribution and the resulting radiation duration.

Intensity I is shown as solid lines in Fig. 4(c) and (d), indicating the duration time is $20\tau\Omega_{ce}$ for Run C and $200 \sim 400\tau\Omega_{ce}$ for Run D with single peak. Since the initially applied electromagnetic field is linearly polarized, we expect that the radiation is also strongly polarized, with the small depolarization coming from the initial random velocity distribution in the

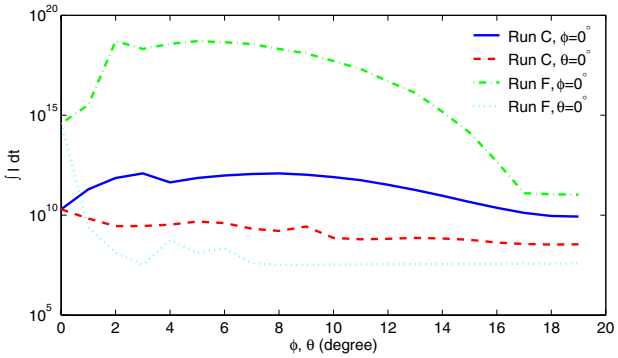

Figure 5: The total radiation intensity $\int I(\phi,\theta)d\tau$ for Run C and Run F as a function of the angle (ϕ,θ).

y direction. Polarization Π is shown as dotted lines in Fig. 4(c) and (d), illustrating that the radiation is strongly linear-polarized as anticipated.

In Fig. 5, we show the total radiation intensity $\int I(\phi,\theta)d\tau$. The radiation is a very short pulse in Fig. 4 because we consider single simulation box centered at the origin only. However, because of the periodic boundary condition in the z direction, we should consider the multiple simulation boxes along the z axis, and consider time delay and angle difference toward the observer from each simulation box, which is very complex even in the Cartesian coordinate.

Instead of including these geometrical effects into the intensity calculation, we simply compare the total intensity integrated over t as a function of the angle. Intensity peaks around $\theta = 3 \sim 8^\circ$ in $\phi = 0$ cases (solid and dash-dot lines), corresponding to the direction of high energy particles in Fig. 2. Intensity rapidly decreases with both ϕ and θ, indicating radiation is strongly collimated in the x direction.

Intensity distribution in the z direction is due to the initial electric field acceleration, as we discussed. Since there is no acceleration in the z direction after the induced current is formed, eventually all the momentum in the z direction will be emitted away, which narrows the intensity distribution toward positive x direction. At the same time, however, decoupling of particles from EM pulse in the x direction makes the DRPA less efficient in the x direction, which widen the distribution. Thus, the intensity in the $x-z$ plane is always distributed over a finite angle, but the distribution in much later time is still an open question.

5. SUMMARY

In summary, we observed the self-consistent radiation damping effect on the interaction of the DRPA with electron-positron plasma via a relativistic PIC simulation. We have found that field and particle energies are transferred to radiation, and the coupling between the field and particles becomes less efficient with larger radiation damping. Comparison with the non-radiative case showed that radiation damping force decelerates the energetic particles accelerated by the DRPA, and resulting radiation power is smaller in the radiative case. The radiation field is strongly linearly polarized both in weak and strong magnetic field cases, which may be detectable by γ-ray burst observations or laser experiments as an indication of the DRPA mechanism. The simulations shown here are too short to see multiple peaks in an intensity time profile as seen in GRB observations, and to determine the final radiation pattern after particles are completely decoupled from EM pulse. These two questions remain as future problems.

Acknowledgments

This research is partially supported by NASA Grant No. NAG5-9223 and LLNL contract nos. B528326 and B541027. The authors wish to thank ILSA, LANL, B. Remington and S. Wilks for useful discussions.

References

[1] E. Liang, K. Nishimura, H. Li, and S. P. Gary, Phys. Rev. Lett. **90**, 085001 (2003).
[2] A. Zhidkov et al., Phys. Rev. Lett. **88**, 18 (2002).
[3] L. Landau and E. M. Lifshits, *The Classical Theorey of Fields* (Pegramon, New York, 1975).
[4] F. Rohrlich, Phys. Rev. A **283**, 276 (2001).
[5] J. D. Jackson, *Classical Electrodynamics* (Wiley, New York, 1975), 2nd ed.
[6] G. B. Rybicki and A. P. Lightman, *Raidiative Processes in Astrophysics* (Wiley-interscience, New York, 1979).
[7] C. K. Birdsall and A. B. Langdon, *Plasma Physics via Computer Simulation* (McGraw-Hill, 1985).